

Radar-Based Multisensor Fusion for Uninterrupted Reliable Positioning in GNSS-Denied Environments

Emma Dawson[✉], Marwan A. Rashed, Walid Abdelfatah, and Aboelmagd Noureldin[✉], *Senior Member, IEEE*

Abstract—Multi-sensor integration is necessary to provide high-precision navigation solutions for autonomous vehicles. Land-vehicles often rely on global navigation satellite systems (GNSS) to acquire its position. However, there are some environments where GNSS signals are unavailable, such as indoor-parking garages, tunnels, and under bridges. Additional sensors are required to allow reliable positioning regardless of location. The vehicle's on-board low cost inertial sensors (accelerometers and gyroscopes) are used for positioning in GNSS-denied environments. Despite their fidelity in short-term usage, inertial navigation systems (INS) are susceptible to drifts in their positioning solution due to the inherent inertial sensor errors, causing positioning errors over time in prolonged scenarios, such as indoor-parking garages. Modern land-vehicles can be equipped with a diversified set of perception systems (e.g. LiDAR, cameras) to provide information about the surrounding environment. These systems are well-studied in literature to provide accurate positioning. Yet, the performance of these systems may degrade in weather conditions such as heavy snow or rain, and may fail in degraded vision environments. The proposed research addresses some of the limitations of current positioning technologies for land vehicles by integrating low-cost on-board motion sensors with the all-weather electronic scanning radar (ESR) systems presently used in adaptive cruise control. This research employs a method of estimating the vehicle position based on multiple ESR systems. Integration with the on-board motion sensors guarantees continuous positioning estimation for uninterrupted navigation. The multi-sensor system integration utilizes extended Kalman filter (EKF) with a unique dynamic tuning approach for reliable and uninterrupted positioning. The proposed solution was examined in real GNSS-denied scenario of an indoor parking. This research has reached an uninterrupted self-contained EKF-based multi-sensor positioning system providing less than 2m error 90% of the time in a GNSS-denied environment for up to four minutes.

Index Terms—Positioning, GNSS, INS, automotive radars, ESR, static object detection, RANSAC, data analysis.

I. INTRODUCTION

LAND VEHICLE positioning methods can be broadly divided into two categories: dead reckoning and position

fixing [1], [2]. Dead reckoning uses a known starting position and information about the direction and speed of a vehicle to calculate an updated position. Position fixing methods (such as global navigation satellite systems (GNSS)) determine the position of a vehicle by measuring its distance to known reference points, and does not need information about the previous position of the vehicle. Most of the present vehicle navigation systems rely on GNSS receivers including the global positioning system (GPS) for positioning services [3]. However, in urban areas GNSS accuracy is limited due to multi-path effects, poor satellite geometry and signal blockage due to high-rise buildings [4], [5].

A. Problem Statement

GNSS is accurate over the long term but its positioning service is degraded in GNSS-denied environments. In situations where the GNSS signal is unreliable or unavailable, it is necessary to have additional sensors participating in the vehicle's ego-motion estimation [6]. The Inertial Navigation System (INS) is a self-contained system based on three accelerometers and three gyroscopes. This grouping of sensors is called an inertial measurement unit (IMU). From the obtained linear acceleration and angular velocities, a dead reckoning positioning solution can be derived [7]. This is most often implemented using the strap-down navigation algorithm to transform the measured body frame accelerations from the body frame to a local level navigation frame. The accelerations are then integrated twice to provide the vehicle's change in position [8].

INS is accurate over short periods of time, but in the long term the inherent sensor errors accumulate leading to unbounded position drift [7]. Furthermore, the cost of highly accurate INS, which utilize high-end high cost IMUs, can be prohibitive to commercial use [6].

Many platforms employ LiDAR and cameras to augment the GNSS/INS positioning solution [9], [10] [11]. LiDAR provides high-resolution perception data, but its reliability deteriorates in weather conditions such as rain and fog. It is also still prohibitively expensive for use on commercial vehicles. Cameras are inexpensive but perform poorly when subjected to poor lighting or in heavy rain, snow or fog conditions [12], [13]. Radars are another low-cost system which are increasingly being used for Advanced Driver-Assistance Systems (ADAS) [14]. Its performance is not affected by poor lighting or weather conditions, although it is not typically used for ego-motion estimation problems [15].

Manuscript received 7 June 2021; revised 25 March 2022, 8 June 2022, and 12 August 2022; accepted 23 August 2022. Date of publication 2 September 2022; date of current version 5 December 2022. This work was supported by a Grant from the Natural Sciences and Engineering Research Council of Canada (NSERC) under Grant RGPIN-2020-03900. The Associate Editor for this article was S.-H. Kong. (*Corresponding author: Emma Dawson.*)

Emma Dawson, Marwan A. Rashed, and Walid Abdelfatah are with the Department of Electrical and Computer Engineering, Queen's University, Kingston, ON K7K 3C2, Canada (e-mail: emma.dawson@queensu.ca).

Aboelmagd Noureldin is with the Department of Electrical and Computer Engineering, Royal Military College of Canada, Kingston, ON K7K 7B4, Canada.

Digital Object Identifier 10.1109/TITS.2022.3202139

1558-0016 © 2022 IEEE. Personal use is permitted, but republication/redistribution requires IEEE permission.
See <https://www.ieee.org/publications/rights/index.html> for more information.

B. Motivation

Increasingly in the automotive industry, cars are being equipped with radar sensors. Automotive radars provide information about the objects in the environment. This information includes distance (range), speed and, depending on the configuration of the system, bearing angle [16]. These automotive radars are low cost, and currently being used in ADAS as well as Adaptive Cruise Control (ACC) [17]. However, these radars are of growing interest in the positioning and navigation fields. Electronic Scanning Radar (ESR) is a type of multiple antenna radar frequently used in land vehicles [18]. A standard low cost ESR returns target detections within a 2-dimensional field of view dependent on the model of sensor, including range, Doppler velocity, and azimuth for each object in the scan [19]. It is therefore possible to use ESR to extract static objects from the environment, and to subsequently use information from these static objects to develop a radar-based positioning solution. As the measurement accuracy of radar technology increases, and the use of radar in the automotive field increases, positioning using radar is a growing area of interest [20]. The low-cost nature of ESR, as well as its robustness to changing weather and lighting conditions, makes it a practical solution to mitigate the drift seen by inertial positioning systems when GNSS is unavailable.

Radar-based odometry is a dead-reckoning system and will consequently accrue drift. However, it aid INS to bridge scenarios where there is no fixed positioning method available. This can mean no GNSS, but also includes instances where no map of the surroundings is available. In parking garages, there can be gaps in the map between the floors, for instance. It is important for there to be an all-weather sensor available to aid the inertial navigation system during these times.

A multi-sensor system fusion scheme relying on ESR and INS has the potential to enhance the performance of the positioning solution in GNSS denied environments.

C. Contributions

The ultimate goal of this research is to propose a multi-sensor positioning and navigation system using radar and inertial technology for GNSS-denied and degraded vision environments. The contributions of this work are summarized as follows:

- A mechanization of a Reduced Inertial Sensor System in a local Cartesian frame
- An analysis of conditions that affect the reliability of positioning using automotive radar and assess the robustness of the integrated solution
- A demonstration of radar odometry and onboard motion sensor fusion on data collected in the real-world driving scenario of a GNSS-denied parking garage

D. Significance

The work presented is demonstrated on real road-test data from radar systems installed in a land vehicle, collected inside a parking garage. This is an important driving scenario and an example of a fully GNSS-denied environment. This research

is also important for positioning solutions in degraded vision environments.

E. Related Work

Using ESR, there are several methods studied in literature for the estimation of a radar sensor's motion. ESR positioning methods can be divided broadly into single scan and adjacent scan methods. Common to all methods is the need to separate detections of static objects from detections of dynamic objects, e.g. moving cars and pedestrians [21]. The relative velocity and position of an object are only useful as an indicator for the sensor's own velocity if that detected object is not moving. Single scan methods consider one scan per iteration and use the detected radial (Doppler) velocities of objects to estimate the motion of the sensor [6], [20]. Adjacent scan methods consider two adjacent scans and attempt to associate objects detected in the first scan to objects detected in the following scan. [6] show a static object detection method using one frontal radar. The algorithm considers the distribution of the azimuth and Doppler velocities of detected objects to eliminate moving objects. The largest group of objects with the same linear movement is assumed to be the group of static objects. This research group extended their technique to two frontal radar in [20], and presented a method to resolve vehicular yaw rate and velocity. In [6], [14], and [20], a Random Sample Consensus (RANSAC) algorithm is used to identify the outliers which in this application are detections corresponding to moving objects [22]. Another method using Frequency Modulated Continuous Wave (FMCW) radar to extract static landmarks is shown in [15].

The second broad category for radar-based positioning involves handling the radar scans as a computer vision problem. This involves using feature extraction and scan matching to calculate the differences in position between detected objects, and subsequently the overall position change of the sensor itself [23], [24], [25], [26]. These methods involve at least four radars to generate a point cloud sufficiently large to satisfy the requirements of the algorithms. Several works explore using neural networks to facilitate the matching of noisy radar scans. Using an FMCW mechanically scanning radar, [27] use convolutional neural networks to predict key points in radar scans, followed by point matching and pose estimation. [28] use a deep neural network to learn an artefact free embedding space and then match between consecutive radar scans. Neither of these methods utilize the Doppler information from the radars.

[29] use a combination of single and adjacent scan methods by using Doppler radar to identify static objects, and then registering radar scans to prior radar maps of the environment.

Sensor fusion involving FMCW radars has been explored in [30]. This work uses the reflection from the ground to measure the vehicle's speed. This speed was then used to update the velocity component of the inertial positioning system instead of the speedometer. In [31], a magnetometer is used to compensate for the large errors in angular velocity. [32] fuse data from an IMU with information from Doppler radar to estimate the velocity of a handheld rig and present a method

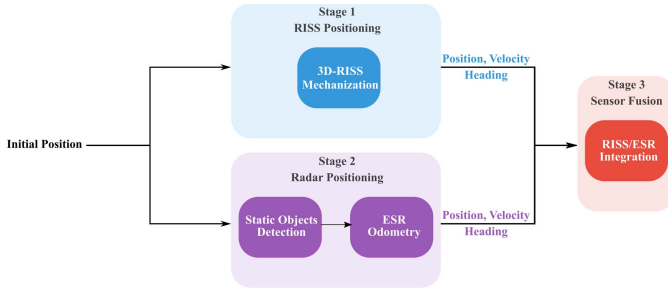


Fig. 1. System overview.

for accumulating radar scans for smoother information. Simultaneous localization and mapping (SLAM) has been explored by extracting features from radar point clouds [33], [34].

II. METHODOLOGY

A. System Overview

The navigation system proposed in this paper relies on automotive ESRs and inertial systems which are already present in many modern vehicles. The system architecture is divided into three main modules: Reduced Inertial Sensor System (RISS) positioning, radar positioning, and sensor fusion. Figure 1 shows the interconnections between the three stages. RISS positioning uses RISS mechanization, an inertial-based dead-reckoning algorithm, to provide 3D position, velocity and heading [35]. Synchronously, the radar positioning module consists of two consecutive sub-blocks: the static objects detection block and the ESR odometry block. The ESR positioning similarly returns a position, velocity and heading estimate. The position, velocity and heading estimates from the RISS module and the ESR module are then passed to the sensor fusion module which employs an EKF to reset the RISS errors and return a robust navigation solution. The random errors associated the RISS positioning solution (system noise) and the radar positioning solution (measurement noise) are both of zero mean and are uncorrelated satisfying the EKF assumption. With each measurement update from the radar positioning, the 3D position errors are estimated, correcting for the computed position solution and feedback to the RISS mechanization for the next processing epoch, guaranteeing proper EKF realization. The proposed ESR/RISS system is a dead reckoning navigation solution, and so it must be initialized using an initial position from which it provides a continuous navigation solution. The three modules are thoroughly explained in section II-B, II-C, and II-D respectively.

B. Reduced Inertial Sensors System (RISS) in Local Cartesian Frame

The position, velocity and heading of the vehicle are represented in a local Cartesian navigation frame which is denoted by X and Y . The body frame coincides with the vehicle frame and is centered at the vehicle's rear axis, where the lateral axis of the body frame is denoted by X_{Body} and the transversal axis of the body frame is Y_{Body} . In both frames of reference, the Z axis is upwards. Fig. 2 describes both frames of reference.

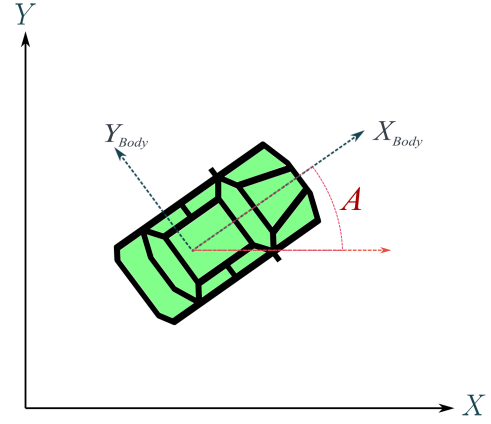


Fig. 2. Navigation and body frames of reference.

The conventional INS mechanization utilizes three accelerometers and three gyroscopes orthogonal to each other [8]. However, to avoid the significant drift of position error associated with the INS solution, we decided to use the RISS mechanization that has proven to be more suitable for land vehicle positioning and navigation [35], [36]. The RISS enhances the traditional INS mechanization by lowering the number of inertial sensors by eliminating two gyroscopes, and utilizing speed measurements from the vehicle speedometer. Unlike the INS where the position is obtained through accelerometers measurements which require two stages of integration, the RISS acquires the position from the odometer v_{od} which requires only one integration, after transforming the measured speed from the body frame to the navigation frame. In addition, RISS only depends on the z -axis gyroscope w_z and eliminates the need for the two gyroscopes along the body frame X and Y axes, which in turn mitigates the biases and the drift accompanying these two gyroscopes. This sensor reduction eliminates the sensor misalignment errors along the body frame X and Y axes that would otherwise propagate into the RISS mechanization process. Instead, to obtain the forward acceleration a_{od} , RISS uses the odometer, and the Coriolis acceleration is obtained by measuring the angular velocity w_z and the forward velocity v_{od} . The RISS block diagram is shown in figure 3.

The RISS used in this research occurs in a local Cartesian navigation frame instead of a global navigation frame, such as the local level frame, which is used in previous works [35]. The modified body frame RISS-based mechanization equations are described in the following subsection.

1) *Attitude Vector Calculations:* The first step in the RISS mechanization is calculating the pitch p and roll r angles. The three orthogonal accelerometers (f_x, f_y, f_z) and the odometer's based acceleration are used to calculate the pitch angle. Yet, only the forward accelerometer f_x and the upward accelerometer f_z are used to obtain the roll angle. Equations (1) and (2) show the pitch and roll calculations.

$$p_k = \arctan \left(\frac{f_{y,k} - a_{od,k}}{\sqrt{f_{x,k}^2 + f_{z,k}^2}} \right) \quad (1)$$

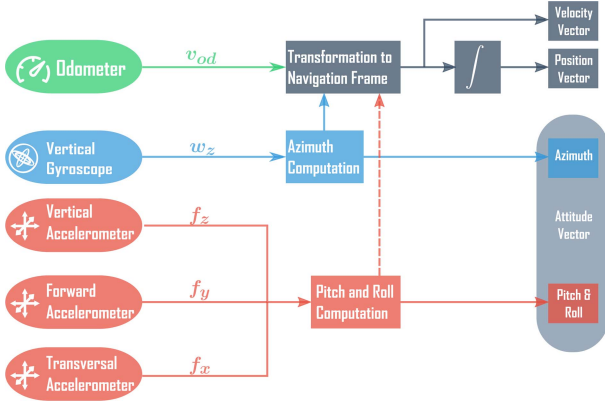


Fig. 3. RISS block diagram.

$$r_k = \arctan\left(\frac{-(f_{x,k} + v_{od,k}\omega_z)}{f_{z,k}}\right) \quad (2)$$

where p_k and r_k are the pitch and roll angles at epoch k , respectively, $f_{y,k}$ is the transversal accelerometer measurement at time epoch k , $f_{x,k}$ is the forward accelerometer measurement at time epoch k , and $f_{z,k}$ is the vertical accelerometer measurement at time epoch k . Finally, $a_{od,k}$ is the odometer based acceleration at time epoch k .

To calculate the heading, the main component is the rate of angular change of the moving platform. The gyroscope bias causes the solution to drift. The bias consists of two components: the deterministic bias offset error ($\delta\omega_z$), and the stochastic drift (b_z). The estimated bias offset component of the gyroscope reading $\delta\omega_z$ is subtracted from the angular velocity in this stage as shown in equation (3). However, the stochastic error drift is modelled and estimated using the EKF in the fusion stage.

$$\omega = \omega_z - \delta\omega_z \quad (3)$$

Once the rate of angular change of the vehicle is calculated, the second step is integrating this value over time to obtain the heading in each epoch. The heading calculation is shown in equation (4).

$$A_{k+1} = A_k + \omega_{k+1} \Delta t \quad (4)$$

where the A_{k+1} is the heading, and ω_{k+1} is the rate of angular change around the vertical axis of the vehicle in the next epoch. A_k is the heading in the current epoch, and Δt is the time between the consecutive epochs.

2) *Velocity Vector Calculations*: The RISS mechanization utilizes the v_{od} to obtain the velocities along the x, y and z axes. These velocities are obtained by the odometer velocity projection using the attitude angles as shown in equations (5,6, and 7).

$$V_{x,k+1} = V_{od,k} \sin(A_{k+1}) \cos(p_{k+1}) \quad (5)$$

$$V_{y,k+1} = V_{od,k} \cos(A_{k+1}) \cos(p_{k+1}) \quad (6)$$

$$V_{z,k+1} = V_{od,k} \sin(p_{k+1}) \quad (7)$$

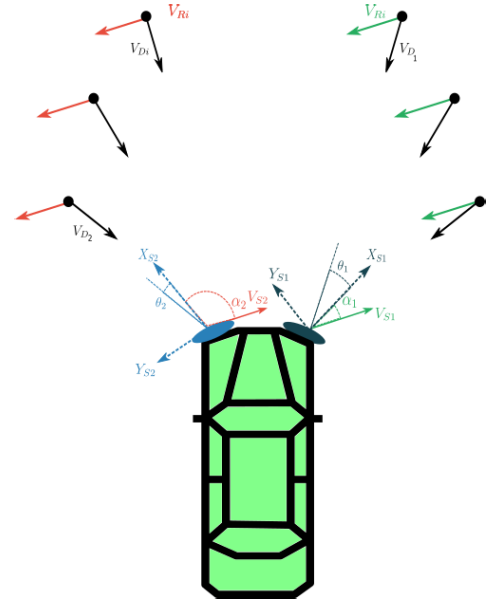


Fig. 4. Ego-vehicle velocity estimation.

3) *Position Vector Calculations*: The velocities along all three axes are integrated to obtain the x, y and z positions. The equations (8, 9, and 10) show the position vector calculations.

$$x_{k+1} = x_k + V_{x,k+1} \Delta t \quad (8)$$

$$y_{k+1} = y_k + V_{y,k+1} \Delta t \quad (9)$$

$$z_{k+1} = z_k + V_{z,k+1} \Delta t \quad (10)$$

C. Ego-Vehicle Velocity Estimation Using Two ESRs

Ego-Vehicle positioning is achieved using a single-scan strategy [20] and two ESRs. This methodology utilizes the azimuth and Doppler velocities of detected objects in each scan to estimate forward and angular velocities for each ESR per epoch. Moving objects are considered outliers, which are rejected in the radar sensor velocity estimation phase using the RANSAC algorithm. RANSAC returns both a radar sensor velocity estimate and flags indicating which objects are inliers to the estimate. Afterwards, the extracted velocities are transformed into the vehicle frame. At the final stage, the transformed velocities are combined to obtain the velocity estimate of the ego-vehicle.

1) *Velocity Estimation of the ESR*: The relationship between sensor velocity and measured Doppler velocities is explained with reference to Figure 4. The two ESR are referenced by identification numbers 1 and 2. ESR_1 is positioned at the front right of the vehicle, angled outwards to the right at approximately -45° , and ESR_2 is positioned at the front left of the vehicle and angled outwards to the left at approximately 45° . Detected objects are represented by the black dots, with their measured Doppler velocities denoted by $V_{D,i}$. The detected azimuth angle for the first object is shown by θ_1 . This is the detection angle with respect to the reference frame of the ESR_1 : (X_{S1}, Y_{S1}) . It should be noted

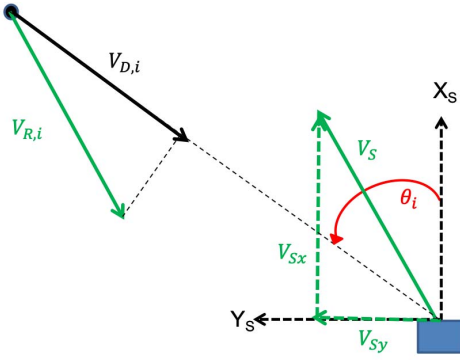


Fig. 5. The doppler velocity as a projection of the relative velocity.

that the Doppler velocities point radially at the ESR. The relative velocities $V_{R,i}$ are equal in magnitude and opposite in direction to the velocities of the radars, denoted by V_{S1} and V_{S2} . The direction of motion of ESR_1 and ESR_2 with respect to their own reference frame is α_1 and α_2 respectively.

The first phase of the ego-vehicle motion estimation methodology is to extract the velocity of each ESR. Consider some static object with detected azimuth and Doppler velocity pair $(V_{D,i}, \theta_i)$. This object will have a velocity relative to the ESR of $V_{R,i}$ with x and y components $(V_{Rx,i}, V_{Ry,i})$. The measured Doppler velocity $V_{D,i}$ of an object is the component of its relative velocity which appears in the direct line between the object and the ESR. In other words, it is a projection of the relative velocity $V_{R,i}$ onto the line between the ESR and the object, as shown in Fig. 5, where X_s and Y_s define the reference frame of the ESR.

The relationship between the Doppler velocity and the relative velocity of a detected object is therefore:

$$V_{D,i} = V_{Rx,i} \cos(\theta_i) + V_{Ry,i} \sin(\theta_i) \quad (11)$$

The relative velocities $V_{R,i}$ of static object detections as compared to the ESR will all be the same. Additionally, the relative object velocities are equal and opposite to the ESR sensor velocity V_s , as shown in 12).

$$V_{R,i} = -V_s \quad (12)$$

Combining (11) and (12), the measured Doppler velocities of static objects can be written in terms of the detected azimuth angles and the x and y sensor velocity components. Equation (13) shows this relationship. For each scan, with the given scan having N object detections, $V_{D,i}$ are the Doppler velocities of objects, θ_i are the detection angles, and V_{Sx} , V_{Sy} are the x and y velocity components of the sensor velocity V_s , with respect to the sensor frame.

$$\begin{bmatrix} -V_{D,1} \\ \vdots \\ -V_{D,N} \end{bmatrix} = \begin{bmatrix} \cos \theta_1 & \sin \theta_1 \\ \vdots & \vdots \\ \cos \theta_N & \sin \theta_N \end{bmatrix} \begin{bmatrix} V_{Sx} \\ V_{Sy} \end{bmatrix} \quad (13)$$

This system of equations can be solved if at least two velocity azimuth pairs $(V_{D,i}, \theta_i)$ are available. For a reliable solution, more pairs must be available, giving an over-defined system of equations. Due to measurement noise and any

dynamic objects potentially present in a scan, this system will not have a perfect solution and must be solved using model-fitting methods for noisy data. This work employs a Random Sample Consensus (RANSAC) algorithm [22] to solve this system of equations for V_{Sx} , V_{Sy} and to reject outliers. The RANSAC algorithm is selected due to its robustness to outliers in the data. As well, it has ability to simultaneously return a solution to the system along with flags indicating which data points are outliers.

2) *Outlier Rejection*: Depending on the environment, detections of moving objects will be included in Eq. 13. The measured velocities of dynamic objects give no information about the velocity of the ego-vehicle [21]. The dynamics of moving objects do not satisfy the relationship between measured Doppler velocity and sensor velocity shown in (13). The dynamic objects are therefore outliers to a model satisfying (13). Even a small number of dynamic targets in a scan will significantly degrade the result of a least squares solution to (13) [6]. It is therefore necessary to solve for the sensor velocities while rejecting objects which are not static. The method used in this paper assumes that the largest group of detections with the same linear velocity will be static objects. All moving objects will be seen as outliers to a model satisfying the Doppler velocities of static objects, and if the static objects form the largest group, it is possible to find such a model using data fitting strategies.

Each iteration of the RANSAC algorithm consists of the following steps [22]:

- 1) Randomly select the azimuth and velocity pairs of two object detections, $(V_{D,i}, \theta_i)$;
- 2) Solve for the sensor velocity (V_{Sx}, V_{Sy}) using least-squares. This provides the current model;
- 3) Using the (V_{Sx}, V_{Sy}) model obtained in the previous step, reverse-solve for all Doppler velocities $(V_{Dmodel,i})$;
- 4) Evaluate the fit of the solution by comparing the error between the solved Doppler velocities $(V_{Dmodel,i})$ with the measured Doppler velocities $V_{D,i}$;
- 5) Flag points that have errors greater than the allowable threshold as outliers;
- 6) Repeat until a model with the maximum number of inliers is found, or until the maximum allowable number of iterations has elapsed.

At the successful completion of the RANSAC algorithm, the (V_{Sx}, V_{Sy}) with the best fit as well as all inliers to the model are returned. Following the completion of RANSAC, the velocities can be re-solved using the inliers returned previously to optimize the result. The error is calculated as the Euclidean distance between the solved Doppler velocities with the measured Doppler velocities. The error calculation has the form:

$$e_i = \sqrt{(V_{D,i} - V_{Dmodel,i})^2} \quad (14)$$

The assumption that the static objects form the largest velocity group is safely satisfied in indoor environments. An example where this assumption may fail is a scenario with many vehicles moving in the same linear direction with the same speed, the RANSAC algorithm could potentially return

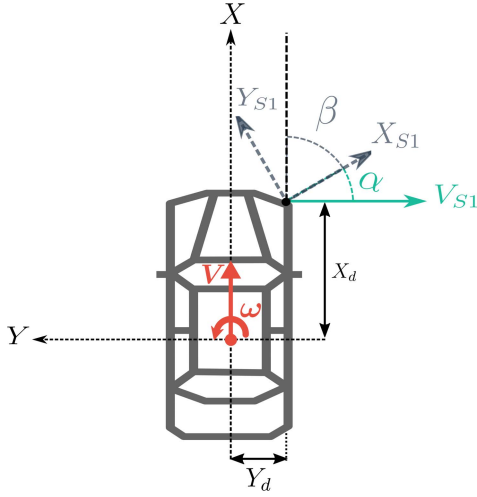


Fig. 6. Velocity transformation.

the speed of the fleet of vehicles instead of the ego-velocity. Another example would be an open area with very few radar detections. In this case, one single passing vehicle could form the largest velocity group. This is a very interesting question for further research.

3) *Velocity Transformation*: The estimated x and y velocity of each ESR can now be transformed to obtain the forward and angular velocity of the vehicle about its centre-rear axle. These velocities are denoted in Fig. 6 by V and ω respectively. The transformation procedure is performed for each of the two ESR, using their individual mounting geometry information as parameters. Fig. 6 shows all variables described in this section for ESR_1 at the front right of the vehicle. The reference frame of ESR_1 is denoted by X_{S1} , Y_{S1} . The reference frame of ESR_1 is rotated by an angle of β compared to the vehicle's reference frame as a result of the mounting angle of ESR_1 on the front right corner of the vehicle. The same procedure applies for ESR_2 , which for clarity is not shown in the figure.

The first step is to compute the angle α , which is the direction of the ESR motion with respect to its own reference frame. This is done using the x and y ESR velocities: V_{Sx} and V_{Sy} . These velocities are the outputs of the RANSAC algorithm described in section II-C.2.

$$\alpha = \arctan(V_{Sy}/V_{Sx}) \quad (15)$$

Next, the magnitude V_S of sensor velocity is computed as shown in equation 16, again using the ESR velocity components estimated by the RANSAC algorithm.

$$V_S = \sqrt{V_{Sx}^2 + V_{Sy}^2} \quad (16)$$

The transformations in (17) and (18) express the sensor velocity V_S in terms of its x and y velocity components in the vehicle frame. In (17) and (18), β is the mounting angle of the ESR with respect to the vehicle frame, and $V_{Sx,vehicle}$, $V_{Sy,vehicle}$ are the x and y ESR velocities in the vehicle frame.

$$V_{Sx,vehicle} = V_S \times \cos(\alpha + \beta) \quad (17)$$

$$V_{Sy,vehicle} = V_S \times \sin(\alpha + \beta) \quad (18)$$

Finally, the x and y ESR velocities are used to obtain the forward and angular velocities of the vehicle, $v_{vehicle}$ and $w_{vehicle}$, in the vehicle frame. The angular velocity $w_{vehicle}$ is about the centre rear axis of the vehicle. These equations are given in (19) and (20). The parameters X_d and Y_d are the mounting positions of the sensor with respect to the centre of the rear axis as shown in Fig. 6. This transformation assumes the Ackerman steering condition, which assumes there is no wheel-slippage. This condition implies that the y velocity of the vehicle at its rear axis is zero.

$$\omega_{vehicle} = \frac{V_{Sy,vehicle}}{X_d} \quad (19)$$

$$V_{vehicle} = V_{Sx,vehicle} - Y_d \times \omega_{vehicle} \quad (20)$$

The estimation of $\omega_{vehicle}$ and $V_{vehicle}$ provide enough information for a standalone ESR dead-reckoning positioning solution.

4) *Combine Information From Multiple ESR*: The method described in Section II-C.3 is performed for each ESR at each timestep. To obtain a robust ESR-based position estimate, the information from each ESR should be combined. Depending on the quality of the ESR scan, the RANSAC algorithm described in Section II-C.2 may return no velocity estimate. If only an estimate from either ESR_1 or ESR_2 is available, then the velocity estimate from the available ESR will be taken alone. If information from both ESR is available, averages of the returned $V_{vehicle}$ and $\omega_{vehicle}$ estimates from ESR_1 and ESR_2 are taken and used as the overall ESR velocity estimate for the vehicle.

5) *Radar-Based Navigation Solution*: All information necessary to construct a radar-based navigation solution is now available. Forward and angular velocities $V_{vehicle}$ and $\omega_{vehicle}$ are used to build a dead-reckoning positioning solution in Cartesian coordinates. At time k , the variables are azimuth A_k , and x and y position x_k and y_k . The timestep is Δt .

The updated heading found using Eq. 21 is an integration of the angular velocity.

$$A_k = A_{k-1} + \omega_{vehicle,k-1} \times \Delta t \quad (21)$$

The updated x and y positions calculated in Eq. 22 and 23 are integrations of the forward velocity multiplied by the sin and cos of the heading angle respectively.

$$x_k = x_{k-1} + V_{vehicle,k-1} \times \cos A_{k-1} \times \Delta t \quad (22)$$

$$y_k = y_{k-1} + V_{vehicle,k-1} \times \sin A_{k-1} \times \Delta t \quad (23)$$

This procedure gives all variables necessary for fusion with INS.

D. Multi-Sensor Fusion Scheme

To reach the best possible positioning accuracy, a multi-sensor fusion scheme is utilized. In the proposed solution, a loosely-coupled Extended Kalman Filter (EKF) is used to fuse the 3D-RISS with the ESR outputs. An EKF is chosen for a number of reasons. First, the dynamic system error model is linearized around the solution provided by the ESR positioning solution, making the higher order terms (representing nonlinearity) insignificant and thus able to be ignored.

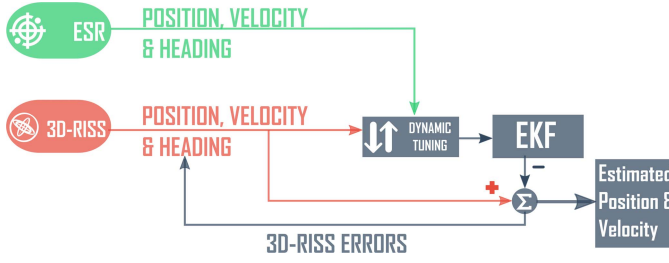


Fig. 7. Extended kalman filter block diagram.

Second, the EKF is the most suitable fusion algorithm when it comes to computation efficiency which is essential for real-time realization. For multi-sensor fusion for positioning and navigation, EKF has been widely used showing to provide high performance with efficient computation that makes it suitable for real-time. [36]. The EKF fusion process is described in Fig. 7. Both the RISS module and ESR module provide position, velocity, and heading. Additionally, the ESR module provides quality indicators such as the number of returned objects in an ESR scan that are used in the dynamic tuning of the measurement covariance matrix. The investigation of the quality indicators is discussed in section III-A. The dynamic tuning phase determines the weighting of the ESR reliability in the fusion process and is further explained in section III. If the ESR is highly weighted, then it is used to estimate and reset the 3D-RISS errors by subtracting the error estimates from the 3D-RISS output, giving the final estimated position and velocity.

The Kalman filter consists of two stages : the prediction stage and the correction stage. The prediction stage contains the system model, while the correction stage includes the measurement model. The utilized scheme has a unique system model, with a distinguished state transition matrix and error state vector, as it is designed for a local-level frame positioning solution.

1) *System Model*: The system model consists of an error state vector δX and a state transition matrix Φ designed for local-level positioning in a Cartesian coordinate frame. The error state vector is a vector of all the navigation state errors, including position errors, velocity errors and heading errors as well as the odometer acceleration errors and the gyro errors. It is defined in Eq. 25. The system model is given in (24), where G_k is the noise distribution matrix and w_k is the process noise, assumed to be White Gaussian Noise (WGN) with zero-mean and covariance Q_k . The system covariance matrix Q represents the variances in the random errors associated with the above error states. It is chosen based on examining the level of uncertainties in the input measurements to the RISS algorithm (e.g. the vertical gyro) and the level of uncertainties in the computed navigation states (e.g. position and velocity).

$$\delta X_k = \phi_{k-1} \delta X_{k-1} + G_k w_k \quad (24)$$

The error state vector δX_k in (24) contains the errors of nine states: the 3D-position x , y and z , the 3D-velocity v_x , v_y , and v_z , and finally the azimuth A , acceleration a_{od} , angular velocity about the upward axis ω_z . The error estimates of these

states are used to correct the 3D-RISS solution when the ESR updates are available. Equation (25) illustrates the error state vector.

$$\delta X = \begin{bmatrix} \delta x \\ \delta y \\ \delta z \\ \delta v_x \\ \delta v_y \\ \delta v_z \\ \delta A \\ \delta a_{od} \\ \delta \omega_z \end{bmatrix} \quad (25)$$

The discrete time state-transition matrix Φ is given by

$$\Phi = I + F \Delta t \quad (26)$$

where I is the 9×9 identity matrix, F is the dynamic state-transition matrix and Δt is the sampling time.

The linearised 3D-RISS error model in a local Cartesian frame is shown in the dynamic transition matrix F in (27), where β and γ are the reciprocals of the autocorrelation time associated with δa_{od} and $\delta \omega_z$. The elements of F are obtained by linearizing the equations of the RISS mechanization presented in Section II-B. This process is well described in [37], with the only difference being that the equations describe latitude and longitude instead of a local Cartesian frame.

$$F = \begin{bmatrix} 0 & 0 & 0 & F_{14} & 0 & 0 & 0 & 0 & 0 \\ 0 & 0 & 0 & 0 & F_{25} & 0 & 0 & 0 & 0 \\ 0 & 0 & 0 & 0 & 0 & F_{36} & 0 & 0 & 0 \\ 0 & 0 & 0 & 0 & F_{45} & 0 & F_{47} & F_{48} & F_{49} \\ 0 & 0 & 0 & 0 & F_{55} & 0 & F_{57} & F_{58} & F_{59} \\ 0 & 0 & 0 & 0 & 0 & 0 & 0 & F_{68} & 0 \\ 0 & 0 & 0 & 0 & 0 & 0 & 0 & 0 & F_{79} \\ 0 & 0 & 0 & 0 & 0 & 0 & 0 & -\beta & 0 \\ 0 & 0 & 0 & 0 & 0 & 0 & 0 & 0 & -\gamma \end{bmatrix} \quad (27)$$

In the F matrix, elements F_{14} , F_{25} , F_{36} and F_{79} have a value of 1. The remaining non-zero elements are:

$$\begin{aligned} F_{45} &= v_y, F_{47} = a_{OD} \cos A \cos(p), \\ F_{48} &= \sin(A) \cos(p), F_{49} = v_y, \\ F_{55} &= -v_y, F_{57} = -a_{OD} \cos A \cos(p), \\ F_{58} &= \cos(A) \cos(p), F_{49} = -v_x, F_{79} = \sin(p). \end{aligned}$$

2) *Measurement Model*: The measurement model allows the radars to aid the RISS solution by resetting its errors. The measurement model is shown in equation (28).

$$z = H \delta X_k + \epsilon \quad (28)$$

where z is the measurement vector with size 5×1 , H is the measurement design matrix with a size 5×9 , and ϵ is the noise of the radar position measurement - White Gaussian Noise (WGN) with zero-mean covariance matrix R . The measurement vector z_{RAD} is the difference between the measured x , y , V_x , V_y , and A states from the ESR and the

RISS navigation solutions.

$$z = \begin{bmatrix} x^{RISS} - x^{RAD} \\ y^{RISS} - y^{RAD} \\ V_x^{RISS} - V_x^{RAD} \\ V_y^{RISS} - V_y^{RAD} \\ A^{RISS} - A^{RAD} \end{bmatrix} \quad (29)$$

Given that the radar solution provides 2D-position, 2D-velocity and the azimuth, the design matrix H is modified and shown in equation (30).

$$H = \begin{bmatrix} 1 & 0 & 0 & 0 & 0 & 0 & 0 & 0 & 0 \\ 0 & 1 & 0 & 0 & 0 & 0 & 0 & 0 & 0 \\ 0 & 0 & 0 & 1 & 0 & 0 & 0 & 0 & 0 \\ 0 & 0 & 0 & 0 & 1 & 0 & 0 & 0 & 0 \\ 0 & 0 & 0 & 0 & 0 & 0 & 1 & 0 & 0 \end{bmatrix} \quad (30)$$

The R matrix carries the variances of the measured states in its diagonal and plays a significant role in the accuracy of the output solution. The R matrix is tuned in order to give weight to either the radar odometry or the RISS solution. Factors that define the confidence level of the ESR system and used to adjust the R matrix are analyzed in section III. The measurement noise covariance matrix is shown in equation (31).

$$R = \begin{bmatrix} \sigma_x^2 & 0 & \sigma_x \sigma_{v_x} & 0 & 0 \\ 0 & \sigma_y^2 & 0 & \sigma_y \sigma_{v_y} & 0 \\ \sigma_x \sigma_{v_x} & 0 & \sigma_{v_x}^2 & 0 & 0 \\ 0 & \sigma_y \sigma_{v_y} & 0 & \sigma_{v_y}^2 & \sigma_{v_y} \sigma_A \\ 0 & 0 & 0 & \sigma_{v_y} \sigma_A & \sigma_A^2 \end{bmatrix} \quad (31)$$

III. DYNAMIC TUNING

The proposed EKF-based fusion method aims to aid the RISS by using the ESR to reset the inertial errors in GNSS-denied scenarios. Since both RISS and ESR navigation systems are dead reckoning positioning solutions, a quality assessment is needed to identify the expected scenarios at which one system may provide higher quality estimates than the other. Consequently, the EKF model should be able to choose when to aid the 3D-RISS using the radar, and when to rely only on the standalone RISS solution. The R matrix as discussed in section II-D.2 is the confidence measurement of the aiding sensor, in this case the automotive ESR. Hence, the R matrix is the component that must be tuned based on the quality of the ESR measurements. Two steps form our dynamic tuning algorithm: the data analysis to identify reliability thresholds, and the smooth fuzzy-based transition between solutions.

A. Data Analysis

The quality analysis of ESR scans is the first step necessary to design the dynamic tuning algorithm. In this phase, some exploratory questions are asked, and answered using the data provided from the radar. The data analysis scheme follows a defined pattern of examining the linear cross-correlation between the variable of interest and errors, followed by the visualized bi-variate relationship between them.

TABLE I
CROSS-CORRELATION BETWEEN NUMBER OF OBJECTS AND ERRORS

Error types	Velocity magnitude	Objects count
Forward velocity error	0.31	0.2
Angular velocity error	-0.01	-0.02

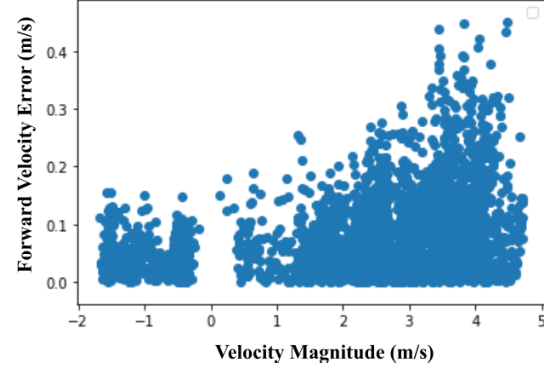


Fig. 8. Relationship between velocity magnitude and forward velocity error.

The main variables of interest are the velocity, the number of objects in the radar scan, and the spatial distribution of the objects around the vehicle. These variables are analyzed statistically against the forward velocity and angular velocity errors taken in comparison to a reference solution. In this step, three main questions are asked:

- Does the vehicle's velocity magnitude affect the error magnitude?
- Does the number of detected objects in a scan have a relationship with the errors?
- What is the effect of the spatial distribution of the objects within a scan on the errors?

To answer the first question, the correlation coefficient between the velocity magnitude and both errors is calculated and shown in Table I. As shown clearly, there is a weak positive relationship of 0.31 between the velocity magnitude and the forward velocity error. Nevertheless, The correlation coefficient between the velocity magnitude and the angular velocity error is almost non-existent with a value of - 0.01. Similarly, the objects count has approximately identical relationships, with a lower coefficient with the forward velocity error of 0.2. This part of the statistical analysis suggests a negligible relationship between the variables of interest and the angular velocity error. However, it shows a slight linear correlation with the forward velocity error suggesting the possibility of useful non-linear relationships that can be further investigated using exploratory data visualization.

Figure 8 shows the forward velocity error of the radar odometry as compared to the reference solution plotted against the forward velocity of the vehicle. The velocity errors are computed by comparing velocity obtained from the radar odometry solution to the reference velocity. It confirms the weak linear correlation between the velocity magnitude and the forward velocity error. However, it shows that as the velocity magnitude increases, there is a higher chance of

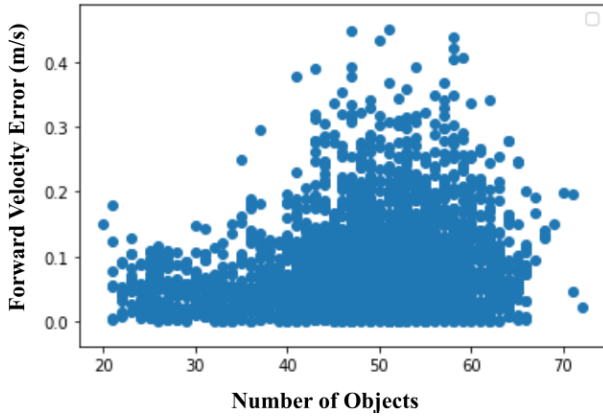


Fig. 9. Relationship between number of objects and forward velocity error.

a larger error. Therefore, error boundaries can be identified based on the velocity magnitudes.

The number of objects in the scan has a visualized bi-variate relationship in figure 9 which suggests that a higher count of objects has higher chance of getting a larger forward velocity error. This contradicts the initial intuitive belief that a high object count should improve the measurement quality due to increased information. Therefore, the statistical analysis of the spatial distribution of the objects must also be conducted to identify if the location of the objects is an important quality aspect or not.

To investigate the spatial distribution of the objects, each point in a scan is categorized based on its location in the scene. The surrounding scene around the vehicle has been divided into 28 rectangular tiles. The maximum distance from the vehicle was chosen based on the maximum range of detections received from the radars. The scene was then divided into smaller tiles near the vehicle and larger ones further away, where fewer detections were observed. The spatial investigation was performed in part to determine whether some areas of a scene are more important than others in the quality of the radar solution. The tiles were smaller in areas of higher object detection density so to maintain a higher resolution for analysis in these areas. Figure 10 illustrates the formulated spatial distribution analysis. The figure shows the intensity of objects in each tile over the whole trajectory. It is clearly observed that 62.8 % of the objects are located in the frontal strip found between the center of the vehicle up to 8 meters longitudinally. The greatest number of objects are located in the overlap-front tile, and the number of objects decreases as we move away from this spot. There are some objects detected behind the vehicle, there should not be as these areas are outside of the field of view of the radars. However, the percentage is small at 0.1%, so this is hypothesized to be due to noise or clutter in the radar measurements.

To follow the defined analysis pattern, the correlation between the number of objects in each tile and the forward velocity error is shown in figure 11. The correlations here are weak.

However, by plotting the velocity error against the object count for the vertical strips of tiles, a non-linear relationship is

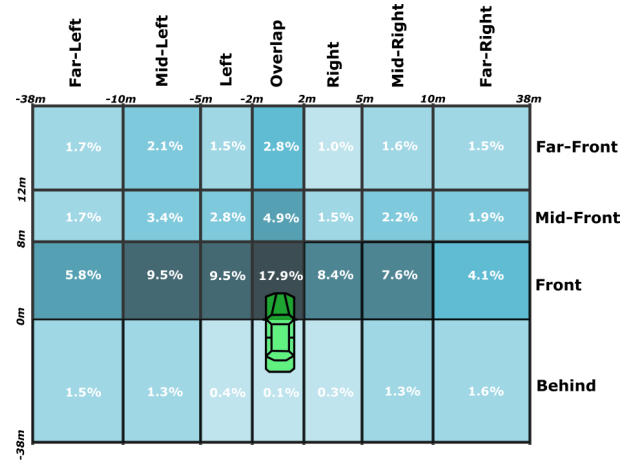


Fig. 10. Number of points intensity over a whole trajectory.

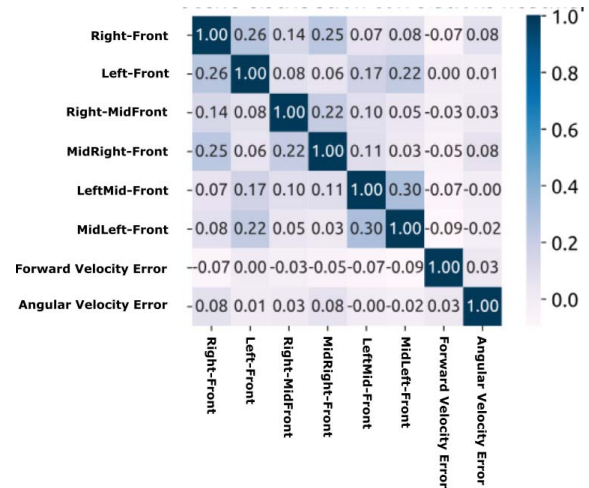


Fig. 11. Cross-correlation between objects distribution and errors.

clearly observed. In Figure 12, for each spatial tile, a decrease in object count leads to an increase in the probability of a high error in both the calculated ESR forward and angular velocities. This distribution has the same shape as the bi-variate relationship between the object count of the entire scan with the velocity errors, as shown in Figs. 8 and 9. However, the tile breakdown lends insight into the tiles which might be more critical in influencing ESR scan quality. A lowering of object count in the Left and Right Front tiles correlates most strongly with an increase in the probability of high velocity error. For the presented trajectory, an object count of 10 in the Right Front tile has a higher maximum velocity error than the Right Middle Front tile does at an object count of 5. A possible conclusion is that a high number of object detections in the Left and Right Front tiles is a critical factor in the fidelity of an ESR scan's calculated velocities. However, this may be misleading because overall there were noted to be fewer detections in these tiles.

B. Tuning Algorithm

From the statistical analysis of Section III-A, a tuning algorithm was developed using the number of objects in the

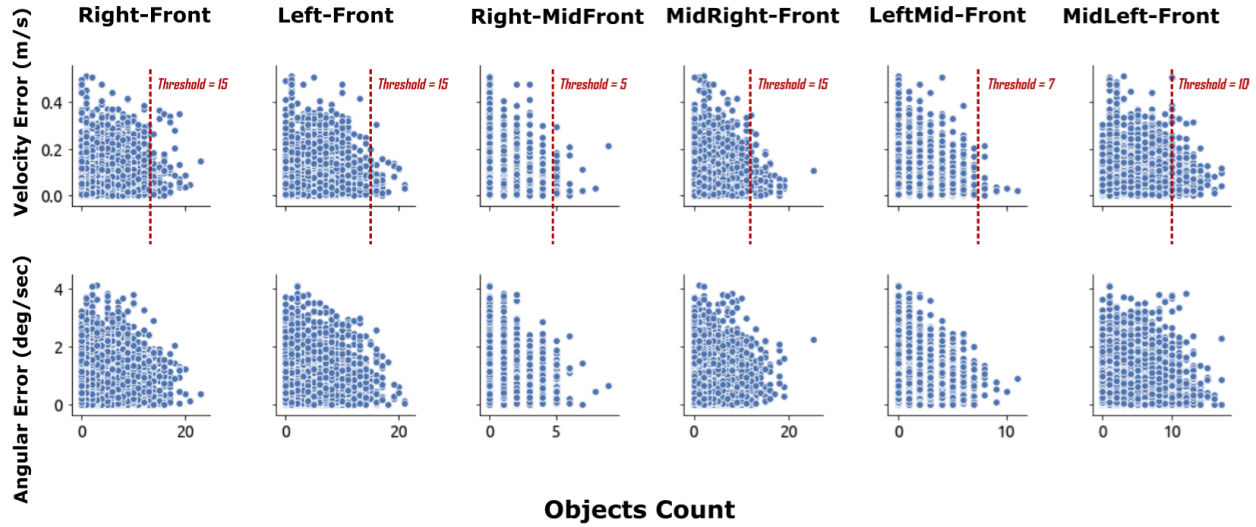


Fig. 12. Relationship between spatial distribution and errors.

Left Front and Right Front tiles per scan as a reliability criterion for the ESR.

It was empirically observed that using ESR scans with fewer detections in these tiles to update the RISS solution leads to a sharp decrease in the quality of the integrated ESR/RISS positioning solution. It can be concluded the number of objects in these tiles is a reliable metric to evaluate the fidelity of an ESR scan. An ESR outage threshold was empirically selected in the distribution of the Left and Right Front tile error distributions. These thresholds are shown as dashed red lines in Fig. 12. Therefore, ESR scans which do not meet the object detection threshold are not used, and the ESR algorithm enters an outage. ESR scans with object detections exceeding the threshold in the Front Left or Front Right tiles undergo an exponential weighting for the EKF using the total number of objects in the ESR scan as a scaling parameter, with scans having a high number of detections being weighted as most reliable in the EKF integration scheme.

When a radar scan has more object detections than the predetermined count threshold, the scan is considered reliable. If the current ESR scan is considered reliable, the RISS algorithm is updated by the ESR solution through the EKF. If the number of object detections drops less than this threshold, the algorithm moves to stand-alone RISS and does not make use of the ESR solution update. The algorithm then commences a timed ESR outage until the number of objects rises above an upper threshold or the outage time elapses, whichever is last to occur. The timed outage is implemented to prevent the algorithm from jumping between RISS-alone and ESR-update fusion, allowing for smoother operation.

The flow of the ESR outage handling algorithm is presented in Algorithm 1. The tuning algorithm checks the ESR outage flag to determine whether or not to use the current radar scan to update the 3D-RISS.

It is important to note that the determined thresholds will be specific to the individual vehicular system, and must be discovered during an initial calibration process. Interestingly, different thresholds were observed for tiles which are

Algorithm 1 Radar Outage Handling

Input: Number of inliers i , threshold $thresh$, time constraint t , current time $time$, current outage status $outage$;

begin

if not $outage$ **then**

if $i < thresh$ **then**

$outage = true$;

$outageStartTime = time$;

end

end

else

$outageDuration = time - outageStartTime$ **if**

$i > thresh \ \& \ outageDuration > t$ **then**

$outage = false$;

end

end

end

symmetric with respect to the body of the vehicle. The tiles are not however symmetric with relation to the environment, because the driver side (left side) radars will be exposed to different object distributions than the passenger side (right side). For example, in the case of these trajectories which occur inside a parking garage, the right side of the car will be much closer to the walls of the garage than the left side will ever be. This will change the distribution of objects in these physically symmetric tiles.

IV. EXPERIMENTAL SETUP

The proposed method is evaluated in two challenging real-world trajectories with distinct dynamics and lengths in indoor parking lot. The experiments were carried out using a testing vehicle equipped with full-sensor suite. All sensors used to collect the data are automotive grade low-cost sensors. The sensors setup is divided into an exterior test-bed and an

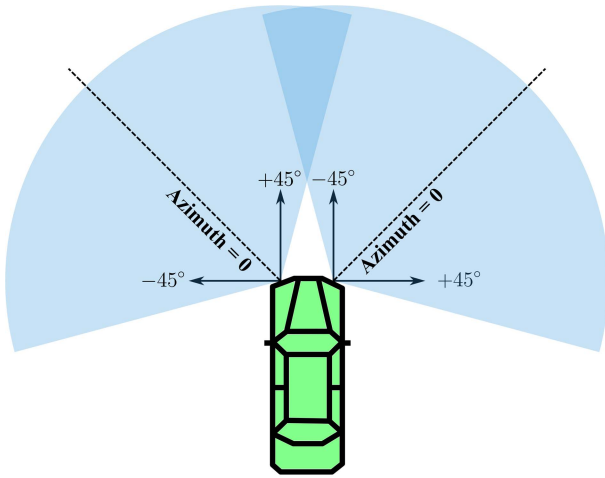


Fig. 13. Vehicle setup.

internal test-bed mounted in the trunk. The internal test-bed includes the on-board vehicle motion sensors. The exterior test-bed consists two ESRs mounted on the sides of the frontal bumper. The ESR is short-range supporting a range from 0.1 m to 100m and a field of view of 150 deg horizontal and 30 deg vertical. It relies on RF CMOS technology and has interference mitigation capabilities and near-field leakage suppression. The ESRs are mounted at approximately ± 45 degree from the vehicle's longitudinal axis. As shown in figure 13, this setup allows the combined ESR system to have a wide field of view.

The automotive radars used have an update rate of 20 Hz, while the inertial sensors provided measurements at 100 Hz and are down-sampled to 10Hz. The vehicle speedometer has an update rate of 100 Hz. Therefore, a synchronization algorithm is used to lower the higher update rates such that the complete positioning system runs at 10 Hz.

The data used in this research was provided by an industry partner and was collected from a passenger car of a certain car manufacturer where professional calibration of the radars was performed. Timestamp synchronization was also performed by the industry partner, and unified time stamps were provided for the radar and the sensor measurements.

The ground truth solution used as a reference for comparison to the odometry solutions is provided by the industry partner supporting this research. It is obtained using advanced algorithms integrating radar point cloud with inertial sensors and registering the point cloud to available 3D maps of the environment.

V. RESULTS AND DISCUSSION

The proposed method is tested on two different real-world trajectories. Both trajectories take place in a multi-level indoor parking building. The trajectories as discussed in the following sub-sections show a diversity in vehicle dynamics, length, and numbers of objects detected. This variety challenges the proposed algorithm in different aspects, resulting to a realistic understanding of the system's merits and weaknesses.

The odometry provides updates at a rate of 10 Hz. Processing at higher data rate (like 100Hz) would provide

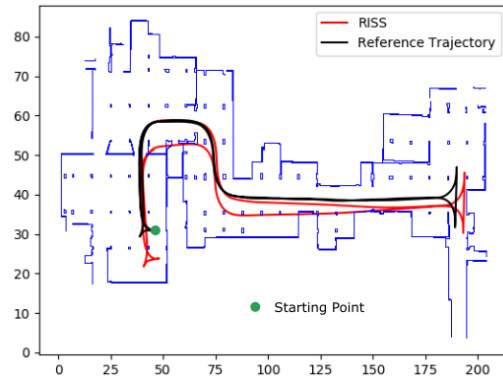


Fig. 14. Trajectory A RISS.

an advantage only if the vehicle moves at high speeds and experiences significant motion dynamics. However, for the purpose of this application and environment (parking garages) the vehicle moves at low speeds. Inertial updates at 100 Hz was tested and did not show any gain in positioning performance due to the limited vehicle dynamics in such environments. Therefore, the decision to operate at a lower data rate was made to make the odometry solution practical and useful for real-time realization, which is an essential requirement for this research project.

A. Trajectory A: Multiple Turns and Reversing

Trajectory A takes place in a single floor indoor parking garage. It starts and ends at the same point to form a closed loop trajectory. To simulate a real scenario of a land-vehicle in a semi-congested parking spaces, the vehicle initiates the trajectory by exiting a parking space. This causes a smooth turn in the first epochs of the trajectory, which could head to an early drift in the inertial or radar positioning outputs. Afterwards, the vehicle goes through a combination of 10 smooth turns, including two reversal movement situations. The trajectory has a duration of 4 minutes, and covers 450 meters in total.

As shown in figure 14, the 3D-RISS positioning is compared to the reference trajectory. Despite the turn at the initial point, the RISS positioning solution does not drift, and is almost conjugate to the reference. The same behaviour continues until the third turn, at which the 3D-RISS begins to drift slightly. Yet, this slight deviation is integrated over time and accumulates with each of the following turns until it reaches the reversing scenario. In the reversing scenario, the inertial positioning deviates completely and the solution terminates approximately 9 meters from the starting point.

Numerically, the 3D-RISS standalone solution has a longitudinal RMS error of 2.21 m, and a maximum of 4.11 m. However, the errors in the lateral position were much higher with a RMS of 4.20 m, and a 7.7m maximum error. Both directions contribute to a 2D-position RMS error of 4.66m, with a maximum of 8.77 meters. These numbers confirm the high-drifting behaviour of the standalone RISS positioning.

Figure 15 shows the enhanced positioning achieved by our proposed EKF-based fusion. In contrast to the standalone

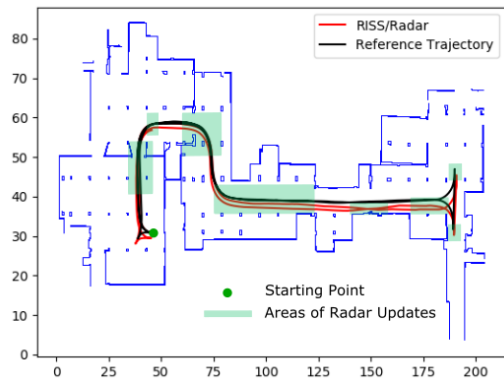


Fig. 15. Trajectory A RISS/Radar fusion.

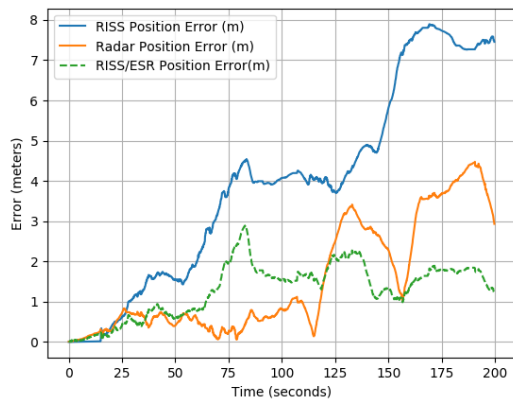


Fig. 16. Position errors over time.

3D-RISS positioning, the fusion shows reliable and consistent behaviour. Fig. 16 shows the 2D position errors over time for the RISS, radar and fused solutions. The fused solution drifts much more slowly than either standalone solution.

In Fig. 15, the radar updates are indicated by the green highlighting. The green highlights cover some segments of the trajectories that the vehicle traverses twice. These radar update decisions occur autonomously through the aid of our developed dynamic tuning algorithm. At the beginning of the trajectory, the 3D-RISS operates alone as the radar measurement does not meet the dynamic tuning criteria. Subsequently, it aids the 3D-RISS two times until it reaches the third turn. The RISS displays a robust behaviour in this area. However, in the third turn the radar meets the specified dynamic tuning criteria, and resets the 3D-RISS errors and gyro biases. As a result, the slight drift present in Fig. 14 was mitigated. The same behaviour continues until the reversal maneuver, at which point the radar corrects the 3D-RISS in two sharp turns, leading to a much better positioning output than the inertial-based solution introduced earlier. On the return journey, the ESR solution updates the EKF at the same segments, resulting a solution nearly conjugate to the reference.

The proposed fusion methodology enhances the standalone 3D-RISS 2D-position RMS error and maximum error by nearly 70 % to achieve 1.5m, and 2.92m, respectively. The RMS longitudinal error is improved to the sub-meter level

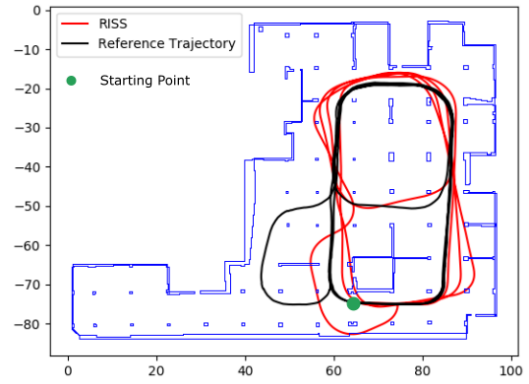


Fig. 17. Trajectory B RISS.

accuracy with an error of 0.71m, and an enhancement of 68 %. Additionally, the 2D-position errors do not exceed 0.60 % of the total distance travelled.

To measure the consistency of the solution, the error level percentage of the travelled distance is presented. The fused positioning methods maintain an error less than 2m 95 % of the time elapsed in the trajectory. Additionally, it is consistently under 1.5 m about 66 % of the trajectory. The solution can achieve a sub-meter level accuracy 60 % of the travelled distance. These numbers demonstrate an effective fusion algorithm. The full results of the trajectory A is shown in table II.

B. Trajectory B: Multiple Loops

Similar to the first trajectory, trajectory B mimics a daily situation of a land-vehicle searching for a parking space in an indoor parking garage. For a period of 5 minutes it performs multiple loops, and covers a wide area of the floor. The first two loops begin and end at the green point in figure 17. The total distanced traveled is 585 meters.

The RISS in figure 17 behaves as expected. It starts following the path of the reference in the straight line, with approximate conjugate positioning output. However, it drifts drastically with the first turn. Unlike the first trajectory, the turns in this scenario are sharper, longer, and repeat more frequently. Consequently, the consecutive loops deviate further from the reference, and the terminal location is approximately 10 meters from the corresponding reference location.

Numerically, Trajectory B shows a poorer performance than Trajectory A. It achieves a 2D-position RMS error of 3.05m after fusion as compared to 1.31m for Trajectory A. Similarly, the pre-fusion system errors are much higher in Trajectory B. The numbers show higher error rates in the lateral axis, which is clearly observed in the figure.

Figure 18 shows the positioning output of the proposed methodology. The performance of the RISS system pre-fusion is very poor in Trajectory B when compared to Trajectory A, both numerically and visually. When compared to the distance travelled and time elapsed during trajectory A, there is more opportunity for error to accrue in trajectory B. The errors can be reduced by number of ways. The first is to use advanced error models for the gyroscope stochastic bias errors together

TABLE II
TRAJECTORY A RESULTS

Error metric	Errors before fusion (m)	Errors after fusion(m)	Enhancement (%)	Error per traveled distance (%)
2D-Position RMS Error	4.66	1.50	68	0.30
2D-Position Max Error	8.77	2.92	67	0.60
X RMS Error	2.21	0.71	68	0.15
Y RMS Error	4.20	1.52	64	0.31
X Max Error	4.11	1.28	69	0.26
Y Max Error	7.70	2.49	68	0.51

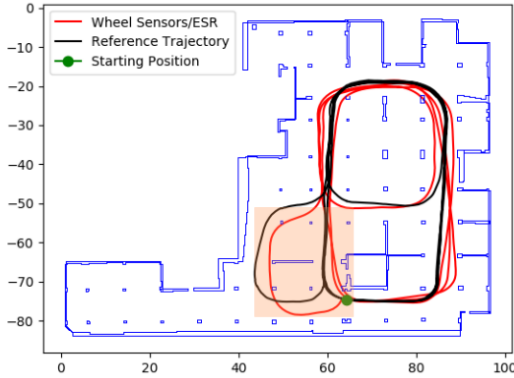


Fig. 18. Trajectory B RISS/Radar fusion.

TABLE III
TRAJECTORY B RESULTS

Error metric	Errors before fusion (m)	Fused errors(m)
2D-Position RMS Error	4.15	3.05
2D-Position Max Error	7.46	5.81
X RMS Error	3.43	2.57
Y RMS Error	2.32	1.66
X Max Error	7.46	5.01
Y Max Error	4.84	2.93

with adding one more state to model the gyroscope stochastic scale factor. The residual errors in the gyroscope contribute to large position errors especially when multiple turns exist in the trajectory. The ESR is a dead reckoning solution, and is unable to fully correct the highly degraded performance of the RISS in Trajectory B. The ESR is used to reset the inertial errors for the entirety of the trajectory. In other words, the EKF dynamic tuning placed high confidence in the ESR. It can be interpreted that the number of objects per scan is higher than the threshold throughout the trajectory. This consistency took place due to the wider space associated with the test environment for Trajectory B.

C. Limitations

This work is limited to tests inside an indoor parking garage, so while it is a real-world scenario of a GNSS-denied environment, we cannot make generalized conclusions for outdoor areas or areas which might include higher vehicle speeds.

VI. CONCLUSION

The work presented in this paper aims to enhance the positioning system of land vehicles in GNSS-denied environments

as demonstrated in an indoor parking garage scenario. Inertial navigation systems (INS) can only support an accurate positioning solution for a brief amount of time before significant position errors are accumulated through integration, leading to large drift. The proposed positioning system is a radar-based multi-sensor positioning method, using two electronic scanning radar (ESR) integrated with INS. The three main modules are the inertial navigation system using a RISS mechanization, the ESR-based positioning system and finally the extended Kalman Filter (EKF) -based integration algorithm. The integration enhances the standalone RISS positioning solution by providing position and heading corrections from the ESR when the radar scans are reliable.

This research develops an integration of RISS with two ESR to provide an uninterrupted and reliable navigation solution for land vehicles in indoor environments. The multi-sensor fusion algorithm mitigates the drift seen by the inertial navigation system over time, allowing for accurate positioning in the absence of GNSS. The RISS is corrected using ESR updates though an EKF-based fusion algorithm. This algorithm dynamically tunes the EKF by assessing the reliability of each radar scan. The reliability of the ESR scan is evaluated based on criterion discovered through a statistical analysis of radar data which is also presented.

The dynamic tuning method presented in this paper results in efficient fusion of both radar and RISS sustaining accurate positioning in GNSS-denied environments. Moreover, the analysis of the distribution of the velocity errors with respect to the number of detected objects and the cross-correlation analysis between the object distribution and errors have not been discussed in previous publications. Another important contribution of the paper is the use of real road test data from radar systems installed in a land vehicle with drive-testing inside a parking garage (a completely denied GNSS environment), which is a unique and important driving scenario. We were able to show a standalone positioning solution based only on measurements from radar and onboard sensors with no GNSS updates for an extended period of time. The analysis and the discussion of the results in Section V on real road test data is another important feature of the paper.

The performance of the proposed system is assessed using two sets of test data referred to as Trajectories A and B in this work. Both trajectories take place in indoor parking garages, and are approximately five minutes long. The trajectories present different dynamics, including multiple tight turns and reversing maneuvers.

This proposed system achieved $< 2\text{m}$ accuracy 90% of the time and $< 1\text{m}$ accuracy 60% of the time. This results in an

enhancement of 70% from the standalone RISS performance. Unfortunately, the performance of the standalone the RISS in Trajectory B is much poorer than that of the ESR, resulting in a fused solution that relies fully on the ESR corrections.

A limitation of the RISS/ESR positioning system is the sparsity of the radar data, which provides an average of 40 detected objects compared to a LiDAR point cloud which numbers in the thousands. Additionally, the algorithm requires that the velocity of each radar sensor be estimated individually before being transformed and combined with the estimates from the other sensors. This is unavoidable in this ESR positioning strategy due to the fact that each sensor has a different velocity profile based on its mounting geometry.

In this work, ESR is used in a multi-sensor fusion system. The results show the capability of radar sensors to be used in positioning applications. The advantages related to the use of ESR over camera and LiDAR include the low cost of the sensor itself, as well as its functionality in all weather and lighting conditions. Additionally, the ESR positioning algorithm is less computationally demanding than LiDAR and cameras because the ESR point cloud is small and the only data required is the Doppler velocity and azimuth of the targets. ESR also does not place any design requirements on the vehicle, unlike LiDAR which must be mounted on the roof of the vehicle. Finally, the presented Doppler velocity -based ESR algorithm is advantageous over scan matching and visual odometry -based ESR methods because it requires less data to perform well. Thus, with the dynamic EKF-based fusion, ESR is a promising sensor for enhancing RISS when GNSS is unavailable.

REFERENCES

- [1] J. Borenstein, H. R. Everett, L. Feng, and D. Wehe, "Mobile robot positioning: Sensors and techniques," *J. Robotic Syst.*, vol. 14, no. 4, pp. 231–249, Apr. 1997.
- [2] P. Groves, *Principles of GNSS, Inertial, and Multisensor Integrated Navigation Systems*, 2nd ed. Norwood, MA, USA: Artech House, 2008.
- [3] M. text Cossaboom textit et al, "Augmented Kalman filter and map matching for 3D RISS/GPS integration for land vehicles," *Int. J. Navigat. Observ.*, vol. 2012, pp. 1–16, Jun. 2012. [Online]. Available: <https://www.hindawi.com/archive/2012/576807/>
- [4] J. Georgy, A. Noureldin, and C. Goodall, "Vehicle navigator using a mixture particle filter for inertial sensors/odometer/map data/GPS integration," *IEEE Trans. Consum. Electron.*, vol. 58, no. 2, pp. 544–552, May 2012.
- [5] U. Iqbal, T. B. Karamat, A. F. Okou, and A. Noureldin, "Experimental results on an integrated GPS and multisensor system for land vehicle positioning," *Int. J. Navigat. Observ.*, vol. 2009, pp. 1–18, Jun. 2009.
- [6] D. Kellner, M. Barjenbruch, J. Klappstein, J. Dickmann, and K. Dietmayer, "Instantaneous ego-motion estimation using Doppler radar," in *Proc. 16th Int. IEEE Conf. Intell. Transp. Syst. (ITSC)*, Oct. 2013, pp. 869–874.
- [7] M. M. Atia, T. Karamat, and A. Noureldin, "An enhanced 3D multi-sensor integrated navigation system for land-vehicles," *J. Navigat.*, vol. 67, no. 4, pp. 651–671, 2014.
- [8] D. H. Titterton and J. L. Weston, *Strapdown Inertial Navigation Technology*. London, U.K.: The Institution of Electrical Engineers, 2004.
- [9] A. Aboutaleb, A. S. El-Wakeel, H. Elghamrawy, and A. Noureldin, "LiDAR/RISS/GNSS dynamic integration for land vehicle robust positioning in challenging GNSS environments," *Remote Sens.*, vol. 12, no. 14, p. 2323, Jul. 2020.
- [10] M. M. Atia, J. Georgy, M. J. Korenberg, and A. Noureldin, "Real-time implementation of mixture particle filter for 3D RISS/GPS integrated navigation solution," *Electron. Lett.*, vol. 46, no. 15, pp. 1083–1084, 2010.
- [11] T. B. Karamat, R. G. Lins, S. N. Givigi, and A. Noureldin, "Novel EKF-based vision/inertial system integration for improved navigation," *IEEE Trans. Instrum. Meas.*, vol. 67, no. 1, pp. 116–125, Jan. 2017.
- [12] T. Chu, N. Guo, S. Backén, and D. Akos, "Monocular camera/IMU/GNSS integration for ground vehicle navigation in challenging GNSS environments," *Sensors*, vol. 12, no. 3, pp. 3162–3185, 2012. [Online]. Available: <https://www.mdpi.com/1424-8220/12/3/3162>
- [13] D. H. Won *et al.*, "Selective integration of GNSS, vision sensor, and INS using weighted DOP under GNSS-challenged environments," *IEEE Trans. Instrum. Meas.*, vol. 63, no. 9, pp. 2288–2298, Sep. 2014.
- [14] R. Saussard, S. Zair, and G. Pita-Gil, "Ego-motion estimation with static object detections from low cost radars," in *Proc. 21st Int. Conf. Intell. Transp. Syst. (ITSC)*, Nov. 2018, pp. 1858–1863.
- [15] S. H. Cen and P. Newman, "Precise ego-motion estimation with millimeter-wave radar under diverse and challenging conditions," in *Proc. IEEE Int. Conf. Robot. Autom. (ICRA)*, May 2018, pp. 6045–6052.
- [16] A. M. W. Menzel, "Antenna concepts for millimeter-wave automotive radar sensors," *Proc. IEEE*, vol. 100, no. 7, pp. 2372–2378, Mar. 2012.
- [17] M. Hoedemaeker, *Driving Behaviour With ACC Acceptance by Individual Drivers*. London, U.K.: IEEE, 2000.
- [18] D. A. Robertson, D. G. MacFarlane, P. A. S. Cruickshank, D. R. Bolton, R. I. Hunter, and G. M. Smith, "High performance mm-wave radar techniques," in *Proc. IET Seminar Digest*, vol. 2006, Jan. 2006, pp. 19–26, doi: [10.1049/ic:20060104](https://doi.org/10.1049/ic:20060104).
- [19] A. Moreira, P. Prats-Iraola, M. Younis, G. Krieger, I. Hajnsek, and K. P. Papathanassiou, "A tutorial on synthetic aperture radar," *IEEE Geosci. Remote Sens. Mag.*, vol. 1, no. 1, pp. 6–43, Apr. 2013.
- [20] D. Kellner, M. Barjenbruch, J. Klappstein, J. Dickmann, and K. Dietmayer, "Instantaneous ego-motion estimation using multiple Doppler radars," in *Proc. IEEE Int. Conf. Robot. Autom. (ICRA)*, May 2014, pp. 1592–1597.
- [21] M. A. Rashed, M. Elhabiby, U. Iqbal, M. J. Korenberg, and A. Noureldin, "Integration of electronic scanning radars with inertial technology for seamless positioning in challenging GNSS environments," in *Proc. IEEE 92nd Veh. Technol. Conf. (VTC-Fall)*, Nov. 2020, pp. 1–5.
- [22] M. A. Fischler and R. C. Bolles, "Random sample consensus: A paradigm for model fitting with applications to image analysis and automated cartography," *Commun. ACM*, vol. 24, no. 6, pp. 381–395, 1981.
- [23] T. Giese, J. Klappstein, J. Dickmann, and C. Wöhler, "Road course estimation using deep learning on radar data," in *Proc. 18th Int. Radar Symp. (IRS)*, Jun. 2017, pp. 1–7.
- [24] F. Schuster, C. G. Keller, M. Rapp, M. Haueis, and C. Curio, "Landmark based radar SLAM using graph optimization," in *Proc. IEEE 19th Int. Conf. Intell. Transp. Syst. (ITSC)*, Nov. 2016, pp. 2559–2564.
- [25] F. Schuster, M. Wörner, C. G. Keller, M. Haueis, and C. Curio, "Robust localization based on radar signal clustering," in *Proc. IEEE Intell. Vehicles Symp. (IV)*, Jun. 2016, pp. 839–844.
- [26] S. H. Cen and P. Newman, "Radar-only ego-motion estimation in difficult settings via graph matching," in *Proc. Int. Conf. Robot. Autom. (ICRA)*, May 2019, pp. 298–304.
- [27] D. Barnes and I. Posner, "Under the radar: Learning to predict robust keypoints for odometry estimation and metric localisation in radar," in *Proc. IEEE Int. Conf. Robot. Automat.*, May 2020, pp. 9484–9490.
- [28] D. Barnes, R. Weston, and I. Posner, "Masking by moving: Learning distraction-free radar odometry from pose information," 2020, *arXiv:1909.03752*.
- [29] L. Narula, P. A. Iannucci, and T. E. Humphreys, "All-weather sub-50-cm radar-inertial positioning," 2020, *arXiv:2009.04814*.
- [30] A. Abosekeen, A. Noureldin, and M. J. Korenberg, "Utilizing the ACC-FMCW radar for land vehicles navigation," in *Proc. IEEE/ION Position, Location Navigat. Symp. (PLANS)*, Apr. 2018, pp. 124–132.
- [31] A. Abosekeen, A. Noureldin, and M. J. Korenberg, "Improving the RISS/GNSS land-vehicles integrated navigation system using magnetic azimuth updates," *IEEE Trans. Intell. Transp. Syst.*, vol. 21, no. 3, pp. 1250–1263, Mar. 2020.
- [32] A. Kramer, C. Stahoviak, A. Santamaria-Navarro, A.-A. Agha-mohammadi, and C. Heckman, "Radar-inertial ego-velocity estimation for visually degraded environments," in *Proc. IEEE Int. Conf. Robot. Autom. (ICRA)*, May 2020, pp. 5739–5746.
- [33] Z. Hong, Y. Petillot, and S. Wang, "Radarslam: Radar based large-scale slam in all weathers," in *Proc. IEEE/RSJ Int. Conf. Intell. Robots Syst.*, Oct. 2020, pp. 5164–5170.
- [34] M. L. Schoen, M. Horn, M. Hahn, and J. Dickmann, "Real-time radar SLAM," in *Proc. Workshop Fahrerassistenzsysteme Automatisiertes Fahren*, 2017, pp. 1–11.

- [35] U. Iqbal, A. F. Okou, and A. Noureldin, "An integrated reduced inertial sensor system—RISS/GPS for land vehicle," in *Proc. IEEE/ION Position, Location Navigat. Symp.*, Jan. 2008, pp. 1014–1021.
- [36] A. Noureldin, T. Karamat, and J. Georgy, *Fundamentals of Inertial Navigation, Satellite-Based Positioning and Their Integration*. Cham, Switzerland: Springer, 2013.
- [37] U. Iqbal, T. B. Karamat, A. F. Okou, and A. Noureldin, "Experimental results on an integrated GPS and multisensor system for land vehicle positioning," *Int. J. Navigat. Observ.*, vol. 2009, pp. 1–18, 2009, Art. no. 765010, doi: [10.1155/2009/765010](https://doi.org/10.1155/2009/765010).



Walid Abdelfatah received the B.Sc. degree in computer engineering from Ain Shams University, Egypt, in 2007, and the M.A.Sc. degree in electrical and computer engineering from Queen's University, Kingston, ON, Canada, in 2010. He has more than ten years of experience in building real-time multi-sensor positioning and navigation products for various applications including pedestrian and land applications. His experience spans embedded systems design, firmware and software development, real-time realization of navigation systems, and managing software and systems teams in fast-paced Agile environments in multiple startups. His research interests include precise positioning technologies using multi-sensors for autonomous vehicles and mobile robots.



mation, and automotive radar fusion.

Emma Dawson received the B.Sc. degree in applied mathematics and engineering from Queen's University, Kingston, ON, Canada, and the M.Sc. degree from the Royal Military College of Canada (RMCC). She is currently pursuing the Ph.D. degree with the Department of Electrical and Computer Engineering, Queen's University. She is also currently working as a Research Assistant at the Navigation and Instrumentation Research Group (NAVINST). Her research interests include sensor fusion, autonomous and vehicular localization, robotic ego-motion estimation, and automotive radar fusion.



fusion, autonomous and vehicular localization, robotic ego-motion estimation, automotive radar fusion, machine learning, deep learning, and machine learning in natural language processing.

Marwan A. Rashed was born in Alexandria, Egypt, in 1995. He received the B.S. degree in mechanical engineering from the Arab Academy of Science and Technology (AAST), Alexandria, Egypt, in 2017, and the M.S. degree in electrical and computer engineering from Queen's University, Kingston, ON, Canada, in 2019. He is currently a Research Assistant with the Navigation and Instrumentation Research Group (NAVINST), jointly at Queen's University and the Royal Military College of Canada (RMCC). His research interests include sensor



Aboelmagd Noureldin (Senior Member, IEEE) received the B.Sc. degree in electrical engineering and the M.Sc. degree in engineering physics from Cairo University, Egypt, in 1993 and 1997, respectively, and the Ph.D. degree in electrical and computer engineering from the University of Calgary, Calgary, AB, Canada, in 2002. Since 2003, he has been a Professor at the Department of Electrical and Computer Engineering, Royal Military College of Canada (RMCC) with Cross-Appointment at both the School of Computing and the Department of

Electrical and Computer Engineering, Queen's University. He is also the Director of the Navigation and Instrumentation (NavINST) Research Group, RMCC. The NavINST Research Laboratory was founded by him with funding from the Canada Foundation for Innovation (CFI), the Ontario Innovation Trust (OIT), and RMCC. He has been a Leader in the field of inertial navigation, global navigation satellite systems, including GNSS, wireless location and navigation, intelligent multi-sensor systems with applications related to positioning and navigation of autonomous vehicles and mobile robot systems; machine learning based human activity recognition and positioning; integrated wireless indoor navigation; intelligent transportation, road information services, crowd management, and the vehicular Internet of Things. He published two books, four book chapters, and over 270 papers in academic journals, conference, and workshop proceedings, in which he received several awards. He is also the Associate Editor of the *Journal of Advanced Transportation* (Hindawi) and the Associate Editor of *Sensors* (MDPI). His research has resulted in active leadership involvement in several projects funded by government and industry, attracting significant research funding and supervising more than 100 highly qualified personnel (HQP) at postdoctoral, graduate, and undergraduate levels. His research work led to 13 patents and several technologies licensed to industry in position, location, and navigation systems. He is a Professional Member of the Institute of Navigation (ION).